Supporting Information

For

Site-isolated redox reactivity in a trinuclear iron complex

Emily V. Eames and Theodore A. Betley*

Department of Chemistry and Chemical Biology, Harvard University
12 Oxford Street, Cambridge MA 02138

Experimental Section

Materials and Methods. All manipulations involving metal complexes were carried out using standard Schlenk line or glove-box techniques under a dinitrogen atmosphere. All glassware was oven-dried for a minimum of 4 h and cooled in an evacuated antechamber prior to use in the dry box. Benzene, diethyl ether, and tetrahydrofuran (THF) were dried and deoxygenated on a Glass Contour System (SG Water USA, Nashua, NH) and stored over 4 Å molecular sieves (Strem) prior to use. Benzene-d_6 was purchased from Cambridge Isotope Labs and were degassed and stored over 4 Å molecular sieves prior to use. Non-halogenated solvents were typically tested with a standard purple solution of sodium benzophenone ketyl in THF in order to confirm effective oxygen and moisture removal. $MeC(CH_2NHPh\text{-}o\text{-}NHPh)_3$ (^{Ph}L) and (^{Ph}L)$Fe_3(THF)_3$ (**1**) were prepared following published methods.[1] Anhydrous pyridine was purchased from Aldrich and stored over 4 Å molecular sieves prior to use. Trityl Chloride was recrystallized from diethyl ether. All other reagents were purchased from commercial vendors and used without further purification unless explicitly stated.

X-ray Structure Determinations. A single crystal suitable for X-ray analysis was mounted and centered on the tip of a cryoloop attached to a goniometer head. Cell parameters were determined using the program SMART.[2] Data reduction and integration were performed with the software package SAINT,[3] while absorption corrections were applied using the program SADABS.[4] Space groups were assigned unambiguously by analysis of symmetry, and systematic absences were determined by XPREP. The positions of the heavy atoms were found via direct methods using the program

SHELXTL.[5] Subsequent cycles of least-squares refinement followed by difference Fourier syntheses revealed the positions of the remaining non-hydrogen atoms. Hydrogen atoms were added in idealized positions. Non-hydrogen atoms were refined with anisotropic displacement parameters. In disordered structures, phenyl rings were constrained to idealized geometries and anisotropic displacement parameters were restrained as necessary. Crystallographic data are given in Tables S1 and selected bond distances and angles in Tables S2-7.

Modeling of Magnetic Data. The susceptibility and reduced magnetization data were modeled using the package MAGPACK.[6] Simulations were run by canvassing a range of parameter values rather than using a fitting algorithm, due to the computational intensity of the calculations. The spin state values reported are the only ones that produced plausible fits, but the exchange, anisotropy and *g* parameters reported should not be taken as definitive, as wide ranges of values gave fits of similar quality. Note: anisotropy parameters are not in general reliably determined by fitting magnetic data. In some cases several plots are shown to demonstrate this (see Figures S13-S15, S17-S18). As described in the text, based on the data from Mössbauer spectroscopy, each trinuclear unit was modeled as a high-spin ferrous unit and a single half-integer spin unit for the Fe_2^{5+} pair, which was determined to be $S = 3/2$ based on the simulations. Satisfactory fits were only obtained using distinct, opposite-sign anisotropy parameters (D) for the two spins within each trinuclear unit, with ferromagnetic coupling between them. For the hexanuclear molecules, satisfactory fits required a small antiferromagnetic coupling through the chloride bridges. Where possible, parameter values were chosen to simultaneously

optimize the fit to the reduced magnetization and susceptibility data, but no attempt was made to optimize the combined fit in a rigorously quantitative way.

---

[1] Eames, E. V.; Harris, T. D.; Betley, T. A. *Chem. Sci.*, **2012**, *3*, 407.
[2] SMART V 5.05 Software for the CCD Detector System; Bruker Analytical X-ray System, Inc.: Madison, WI, 1998.
[3] SAINT. Data Reduction Software. V 6.36A; Bruker Analytical X-ray System, Inc.: Madison, WI, 2002.
[4] SADABS. Bruker/Siemens Area Detector Absorption and Other Corrections. V2.03; Bruker Analytical X-ray System, Inc.: Madison, WI, 2002.
[5] Sheldrick, G. M., *SHELXTL. V 6.12*; Bruker Analytical X-ray Systems, Inc.: Madison, WI, 2000.
[6] Borrás-Almenar, J. J.; Clemente-Juan, J. M.; Coronado, A.; Tsukerblat, B. S. *J. Comput. Chem.*, **2001**, *22*, 985.

Figure S1. UV-vis spectra of **2** in tetrahydrofuran (green) and **6** in tetrahydrofuran (purple). Complex **2** is expected to be in a monomeric thf-bound form in the tetrahydrofuran solution. Near IR studies reveal no additional bands between 1000-1500 nm.

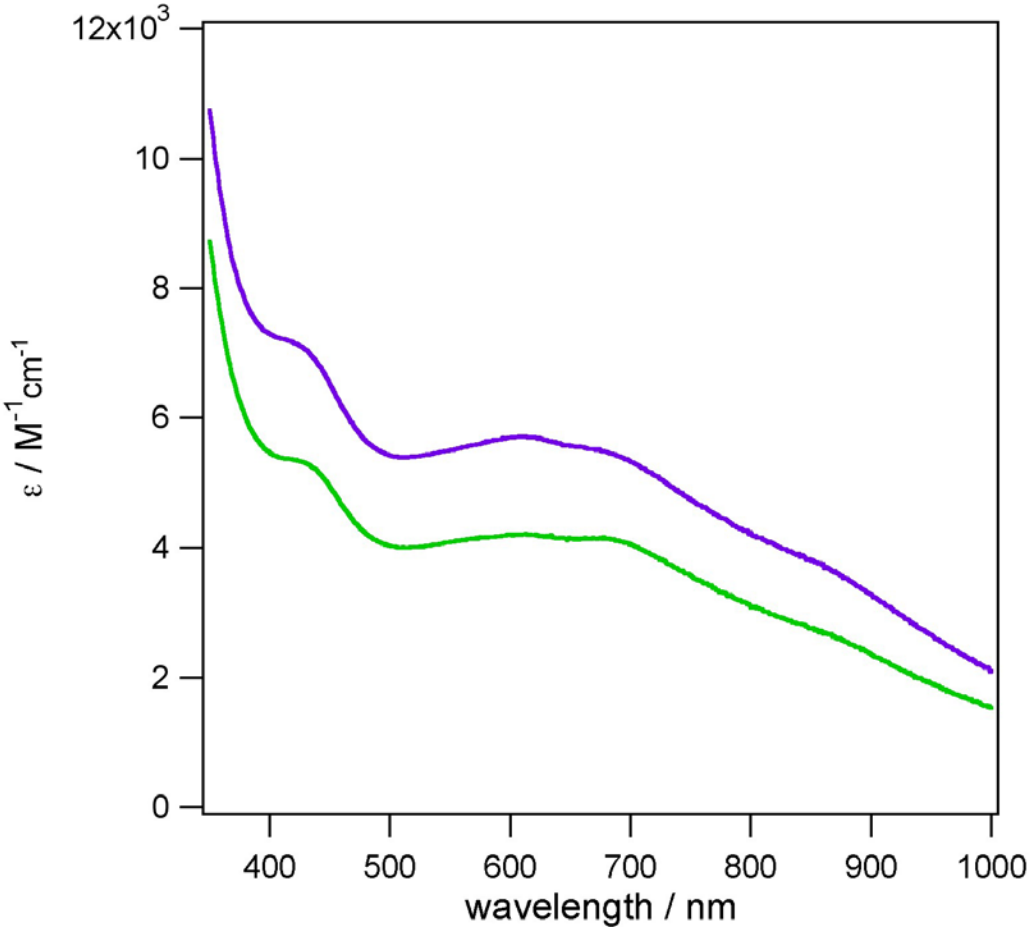

Table S1. X-ray Crystallographic Data for **2-6**.

	2	**3**	**4**	**5**	**6**
Chemical formula	$[C_{41}H_{36}Fe_3Cl]_2 \cdot 3.5(C_6H_6)$	$C_{46}H_{41}Fe_3N_7Cl \cdot (C_6H_6)$	$[C_{41}H_{36}Fe_3Br]_2 \cdot 3.5(C_6H_6)$	$C_{45}H_{44}Fe_3N_6OBr \cdot 3(C_4H_8O)$	$C_{45}H_{44}Fe_3N_6OI \cdot 1.5(C_6H_6)$
FW	1904.89	972.97	1993.81	1148.63	1096.47
Space group	*C2/c*	*P*1bar	*C2/c*	*P2(1)/c*	*P*1 bar
a (Å)	20.5157(19)	10.6400(14)	20.5157(19)	11.6808(8)	12.984(3)
b (Å)	16.5388(15)	13.8195(18)	16.5388(15)	35.637(2)	13.210(3)
c (Å)	26.062(2)	17.468(2)	26.062(2)	12.7385(9)	14.734(3)
α (deg)	90	99.426(2)	90	90	86.701(3)
β (deg)	99.657(2)	103.926(2)	99.657(2)	103.8260(10)	80.278(3)
γ (deg)	90	111.921(2)	90	90	77.288(3)
V (Å^3)	8717.7(14)	2219.1(5)	8717.7(14)	5149.0(6)	2429.3(8)
Z	4	2	4	4	2
d_{calcd} (g·cm^{-3})	1.451	1.456	1.519	1.482	1.499
μ (mm^{-1})	1.091	1.074	1.946	1.664	1.565
T (K)	100(2)	100(2)	100(2)	100(2)	100(2)
R1[a] (wR2[b])	0.0367 (0.1327)	0.0538 (0.1419)	0.0372 (0.0920)	0.0553 (0.1301)	0.0479 (0.1453)

[a] $R1 = [\sum w(F_o - F_c)^2 / \sum wF_o^2]^{1/2}$.

[b] $wR2 = [\sum [w(F_o^2 - F_c^2)^2] / \sum w(F_o^2)^2]^{1/2}$, $w = 1/[\sigma^2(F_o^2) + (aP)^2 + bP]$, where $P = [\max(F_o^2,0) + 2(F_c^2)]/3$.

Table S2. Selected Core Bond Distances (Å) of **2**-**6**.

Temperature (K)	**2**	**3**	**4**	**5**	**6**
Fe(1)–Fe(2)	2.5889(5)	2.7303(8)	2.5871(7)	2.7183(10)	2.6026(10)
Fe(1)–Fe(3)	2.5801(5)	2.6534(8)	2.5871(7)	2.7034(10)	2.6971(11)
Fe(2)–Fe(3)	2.3410(5)	2.2955(8)	2.3504(7)	2.3037(10)	2.3079(10)
Fe(1)–X	2.3573(6)	2.3333(11)	2.4670(6)	2.4475(9)	2.6695(9)
Fe(1)–L	2.4425(6)	2.066(3)	2.5715(6)	2.037(3)	2.024(4)
Fe(1)–N(2)	2.081(2)	2.078(3)	2.085(3)	2.090(4)	2.081(4)
Fe(1)–N(3)	2.092(2)	2.078(4)	2.075(3)	2.097(4)	2.082(4)
Fe(2)–N(1)	1.923(2)	1.924(3)	1.926(3)	1.929(4)	1.970(4)
Fe(2)–N(3)	1.9266(19)	1.914(3)	1.937(3)	1.919(4)	1.909(4)
Fe(2)–N(4)	1.978(2)	1.966(3)	1.994(3)	1.992(4)	2.073(4)
Fe(2)–N(6)	1.8552(19)	1.871(3)	1.862(3)	1.859(4)	1.869(4)
Fe(3)–N(1)	1.965(2)	1.968(4)	1.946(3)	1.954(4)	1.921(4)
Fe(3)–N(2)	1.916(2)	1.900(3)	1.916(3)	1.908(4)	1.924(4)
Fe(3)–N(4)	2.059(2)	2.067(3)	2.059(3)	2.048(4)	1.977(4)
Fe(3)–N(5)	1.872(2)	1.881(4)	1.916(3)	1.889(4)	1.859(4)

Table S3. Selected Ligand Bond Distances (Å) for **2**.

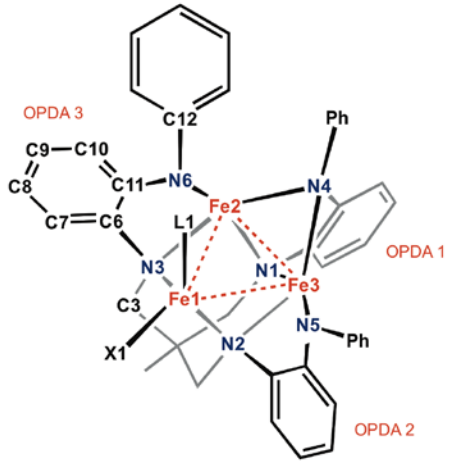

OPDA subunit	**1**	**2**	**3**
C(3)–N(1)	1.465(3)	1.479(3)	1.488(3)
N(1)–C(6)	1.417(3)	1.423(3)	1.431(3)
C(6)–C(7)	1.386(4)	1.389(3)	1.401(3)
C(7)–C(8)	1.389(4)	1.387(4)	1.392(4)
C(8)–C(9)	1.389(5)	1.387(4)	1.398(4)
C(9)–C(10)	1.394(4)	1.395(3)	1.386(4)
C(10)–C(11)	1.386(4)	1.396(3)	1.402(4)
C(6)–C(11)	1.417(3)	1.414(3)	1.407(4)
C(11)–N(4)	1.439(3)	1.387(3)	1.388(3)
N(4)–C(12)	1.429(3)	1.430(3)	1.331(7)

Table S4. Selected Ligand Bond Distances (Å) for **3**.

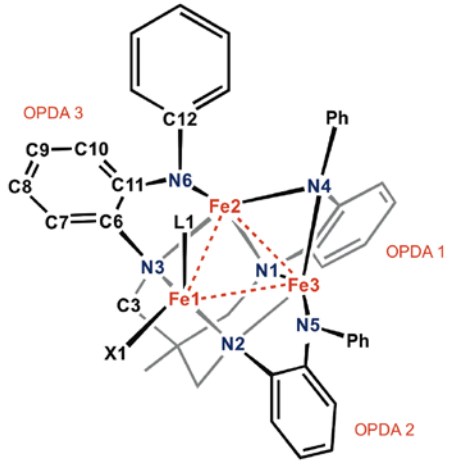

OPDA subunit	**1**	**2**	**3**
C(3)–N(1)	1.460(5)	1.474(5)	1.476(5)
N(1)–C(6)	1.412(5)	1.423(5)	1.434(5)
C(6)–C(7)	1.382(5)	1.385(5)	1.386(6)
C(7)–C(8)	1.388(6)	1.381(6)	1.379(6)
C(8)–C(9)	1.390(6)	1.373(7)	1.391(6)
C(9)–C(10)	1.387(5)	1.378(6)	1.382(6)
C(10)–C(11)	1.385(5)	1.407(6)	1.395(5)
C(6)–C(11)	1.407(6)	1.410(6)	1.413(5)
C(11)–N(4)	1.439(4)	1.387(5)	1.388(5)
N(4)–C(12)	1.427(5)	1.416(6)	1.429(5)

Table S5. Selected Ligand Bond Distances (Å) for **4**. Distances are reported for one subunit only, as the others are disordered and bond distances were constrained to 1.39 Å during refinement.

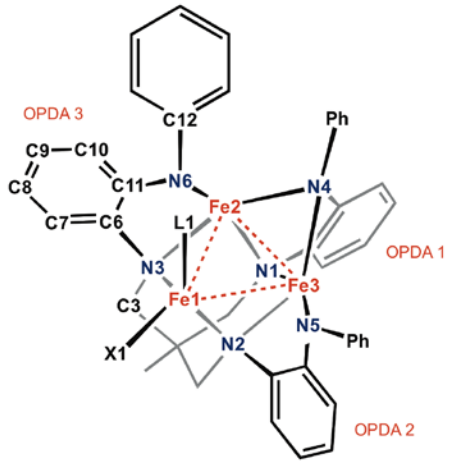

OPDA subunit	**2**
C(3)–N(1)	1.480(4)
N(1)–C(6)	1.426(5)
C(6)–C(7)	1.404(5)
C(7)–C(8)	1.398(6)
C(8)–C(9)	1.382(6)
C(9)–C(10)	1.389(5)
C(10)–C(11)	1.410(5)
C(6)–C(11)	1.412(6)
C(11)–N(4)	1.394(5)
N(4)–C(12)	1.435(4)

Table S6. Selected Ligand Bond Distances (Å) for **5**.

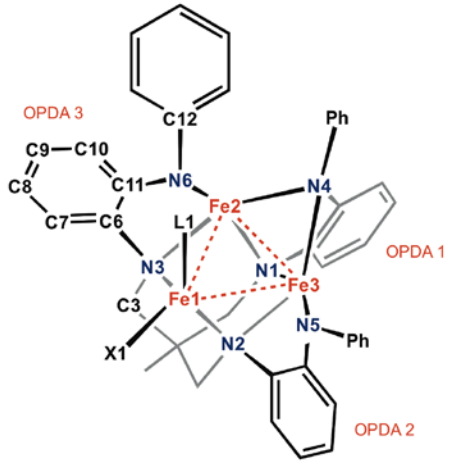

OPDA subunit	**1**	**2**	**3**
C(3)–N(1)	1.468(6)	1.486(6)	1.497(6)
N(1)–C(6)	1.424(6)	1.424(6)	1.431(6)
C(6)–C(7)	1.387(7)	1.391(7)	1.386(7)
C(7)–C(8)	1.393(7)	1.386(7)	1.383(7)
C(8)–C(9)	1.380(7)	1.387(7)	1.374(7)
C(9)–C(10)	1.395(7)	1.390(7)	1.392(7)
C(10)–C(11)	1.384(7)	1.405(6)	1.399(7)
C(6)–C(11)	1.410(6)	1.417(6)	1.409(7)
C(11)–N(4)	1.431(6)	1.373(6)	1.396(6)
N(4)–C(12)	1.441(6)	1.436(6)	1.435(6)

Table S7. Selected Ligand Bond Distances (Å) for **6**.

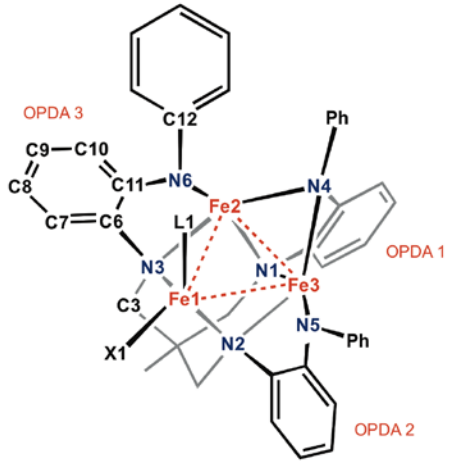

OPDA subunit	**1**	**2**	**3**
C(3)–N(1)	1.452(6)	1.482(6)	1.482(6)
N(1)–C(6)	1.418(6)	1.423(6)	1.417(6)
C(6)–C(7)	1.383(7)	1.410(7)	1.392(7)
C(7)–C(8)	1.389(7)	1.391(7)	1.381(8)
C(8)–C(9)	1.379(8)	1.375(8)	1.398(8)
C(9)–C(10)	1.384(7)	1.388(8)	1.379(8)
C(10)–C(11)	1.394(7)	1.398(7)	1.394(7)
C(6)–C(11)	1.414(7)	1.405(7)	1.410(7)
C(11)–N(4)	1.432(6)	1.394(6)	1.387(7)
N(4)–C(12)	1.426(6)	1.434(6)	1.425(6)

Figure S2. Solid state structure of **2** the thermal ellipsoids set at the 50% probability level (hydrogen atoms and solvent molecules omitted for clarity; Fe orange, C black, N blue, Cl green).

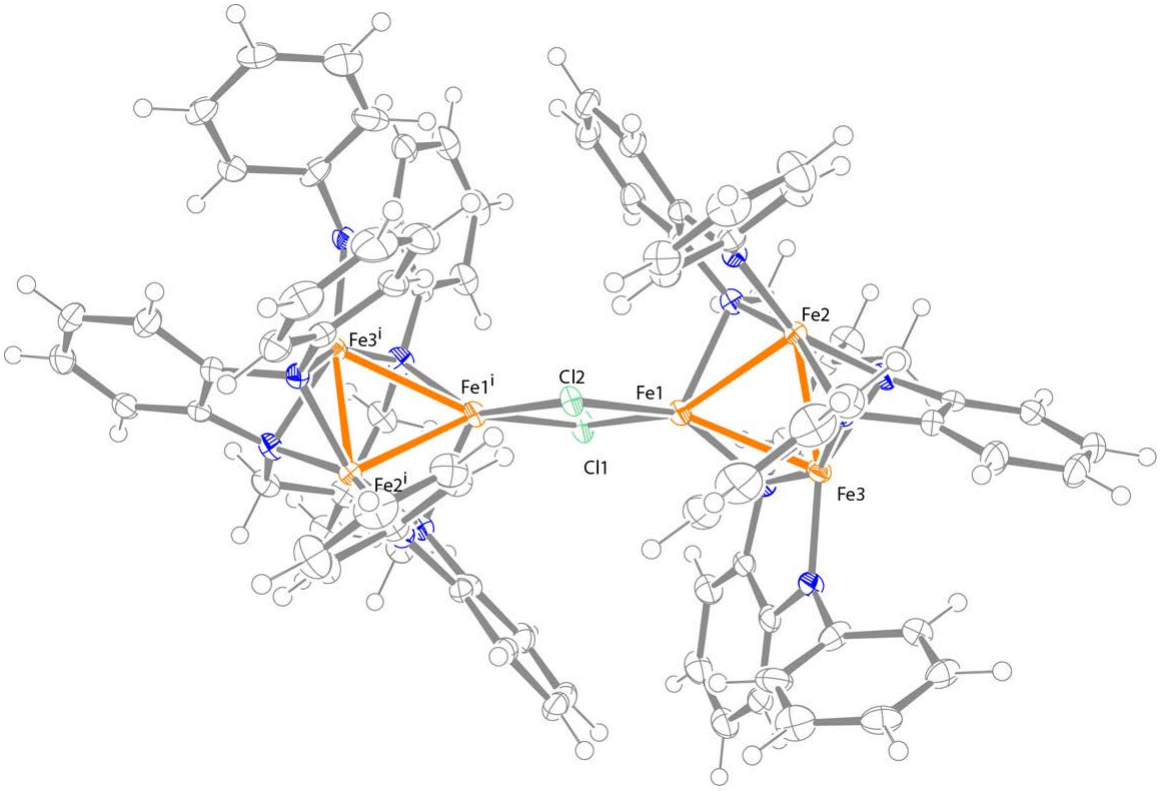

Figure S3. Solid state structure of **3** with the thermal ellipsoids set at the 50% probability level (hydrogen atoms and solvent molecules omitted for clarity; only one site shown for disordered atoms; Fe orange, C black, N blue, Cl green).

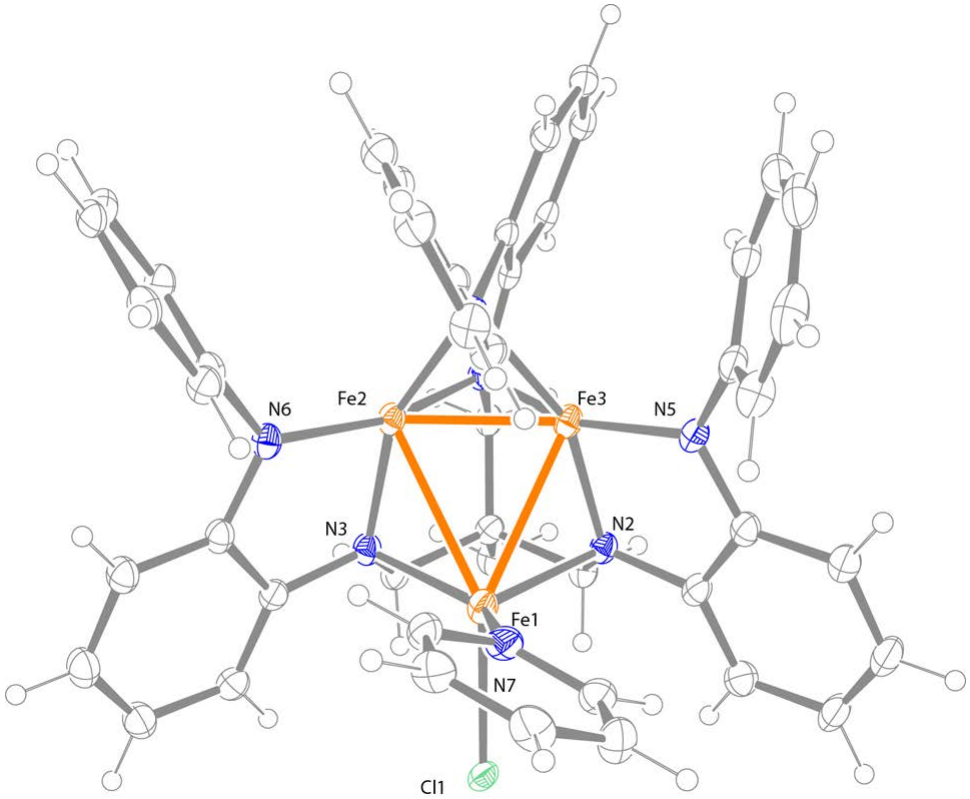

Figure S4. Solid state structure of **4** with the thermal ellipsoids set at the 50% probability level (hydrogen atoms and solvent molecules omitted for clarity; Fe orange, C black, N blue, Br maroon).

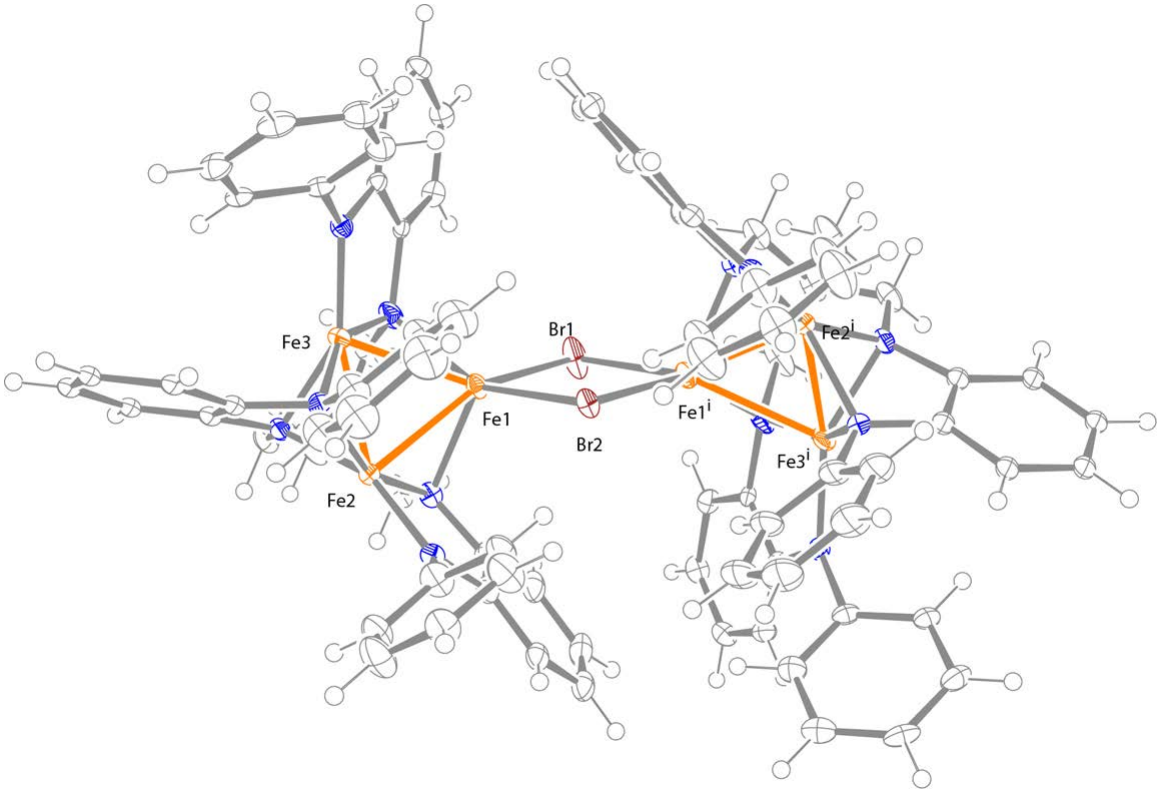

Figure S5. Solid state structure of **5** with the thermal ellipsoids set at the 50% probability level (hydrogen atoms and solvent molecules omitted for clarity; Fe orange, C black, N blue, Br maroon, O red).

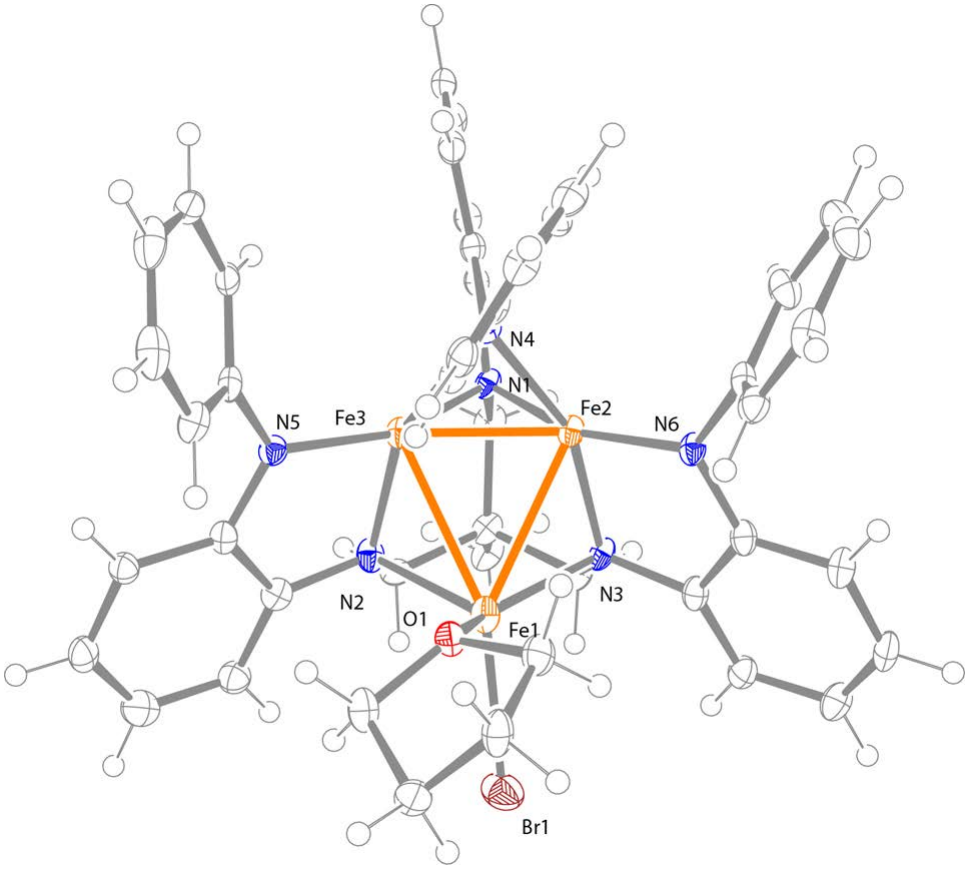

Figure S6. Solid state structure of **6** with the thermal ellipsoids set at the 50% probability level (hydrogen atoms and solvent molecules omitted for clarity; Fe orange, C black, N blue, I green, O red).

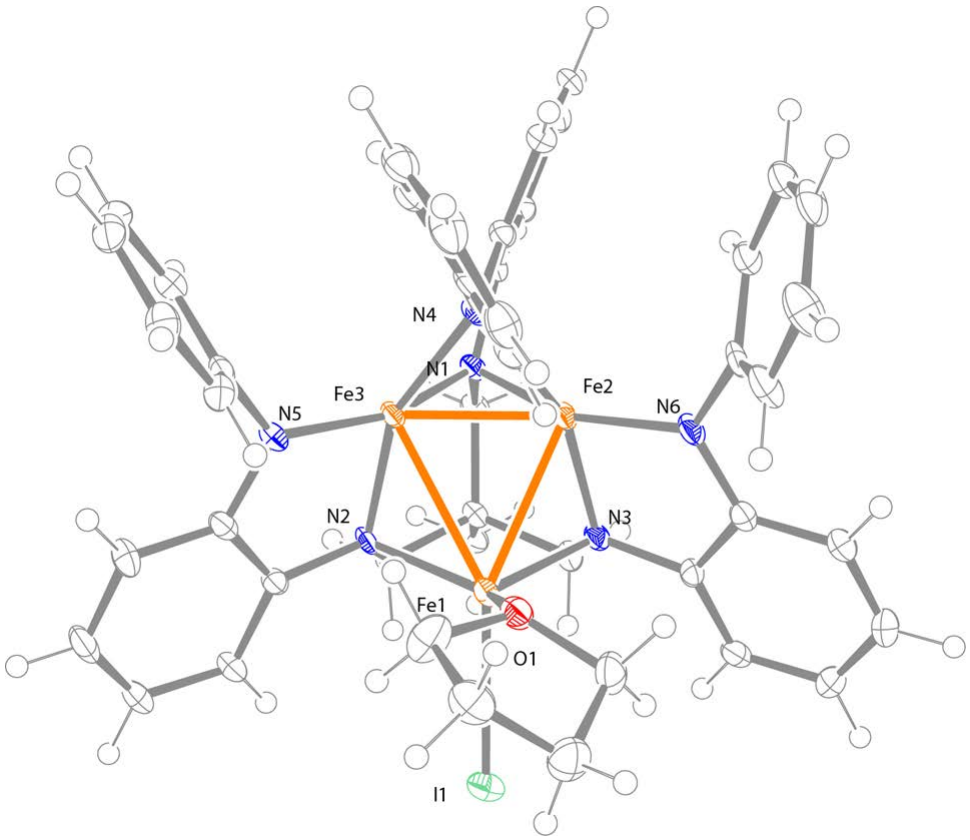

Figure S7. Zero-field ^{57}Fe Mössbauer spectrum of **2**. Simulation yields the following parameters: (blue, 33.3%) δ = 0.22 mm/s, ΔE_Q = 2.72 mm/s, γ = 0.14 mm/s; (green, 33.3%) δ = 0.26 mm/s, ΔE_Q = 2.43 mm/s, γ = 0.23 mm/s; (gold, 33.3%) δ = 0.79 mm/s, ΔE_Q = 1.54 mm/s, γ = 0.18 mm/s.

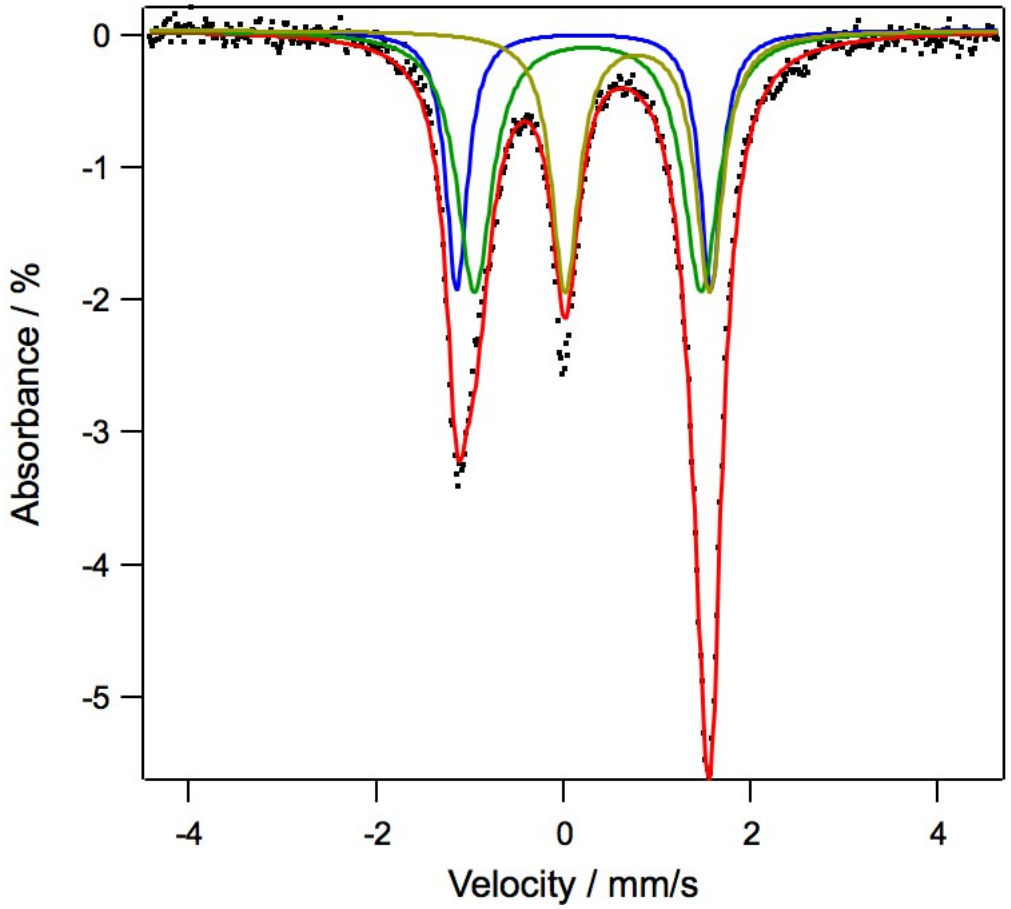

Figure S8. Zero-field ^{57}Fe Mössbauer spectrum of **3**. Simulation yields the following parameters: (blue, 33.3%) δ = 0.23 mm/s, ΔE_Q = 2.86 mm/s, γ = 0.14 mm/s; (green, 33.3%) δ = 0.29 mm/s, ΔE_Q = 2.43 mm/s, γ = 0.14 mm/s; (gold, 33.3%) δ = 0.80 mm/s, ΔE_Q = 1.60 mm/s, γ = 0.13 mm/s.

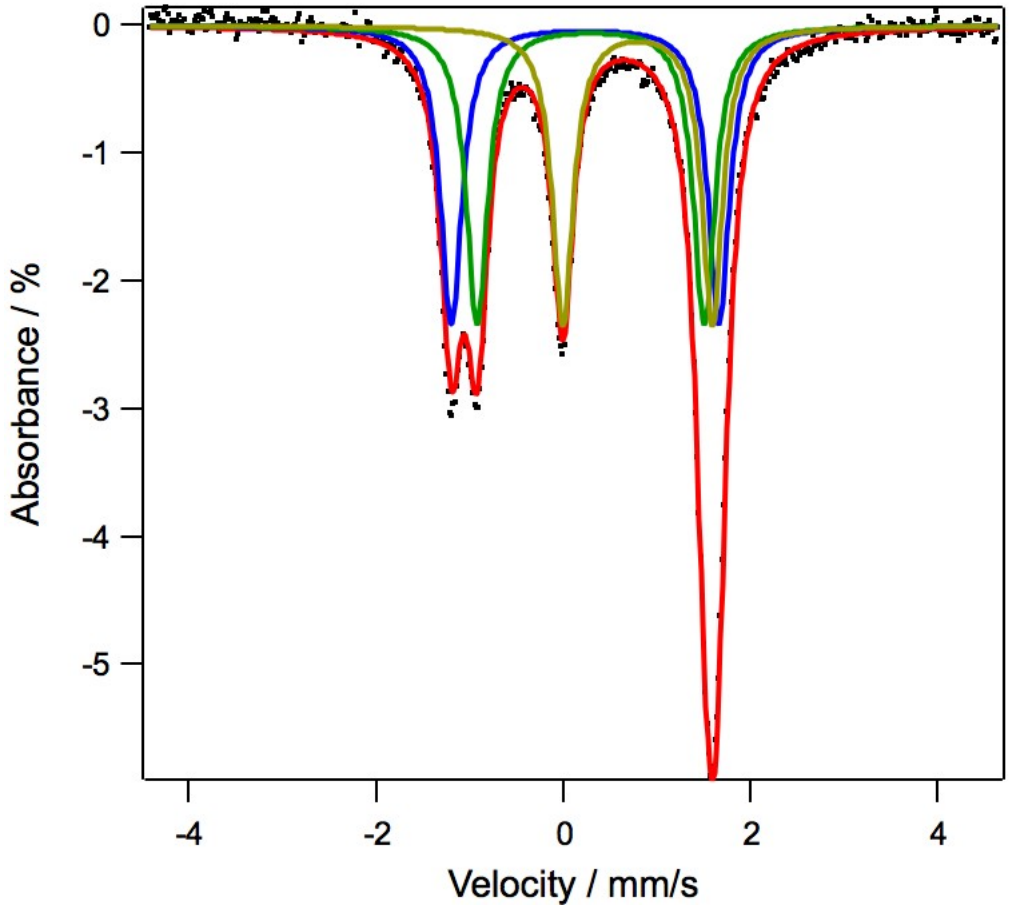

Figure S9. Zero-field ^{57}Fe Mössbauer spectrum of **4**. Simulation yields the following parameters: (blue, 36.2%) δ = 0.22 mm/s, ΔE_Q = 2.76 mm/s, γ = 0.12 mm/s; (green, 31.9%) δ = 0.31 mm/s, ΔE_Q = 2.46 mm/s, γ = 0.13 mm/s; (gold, 31.9%) δ = 0.75 mm/s, ΔE_Q = 1.49 mm/s, γ = 0.14 mm/s.

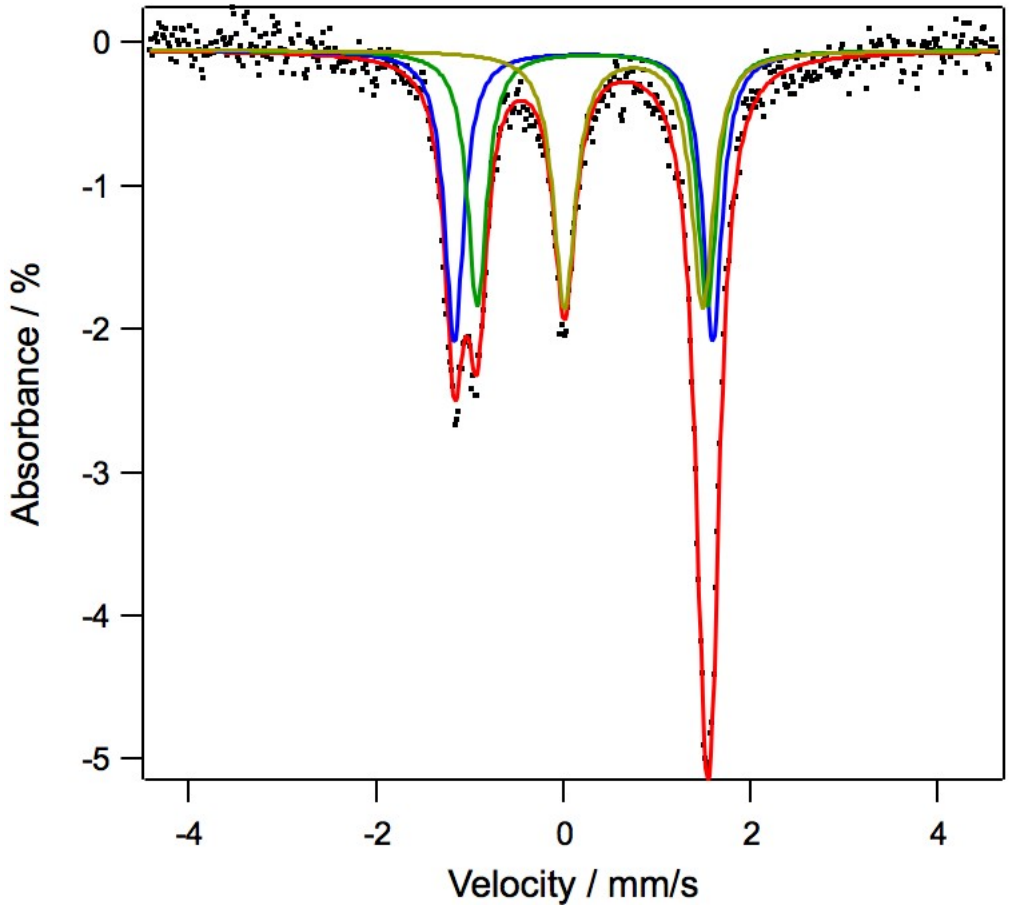

Figure S10. Zero-field ^{57}Fe Mössbauer spectrum of **5**. Simulation yields the following parameters: (blue, 64.0%) δ = 0.26 mm/s, ΔE_Q = 2.76 mm/s, γ = 0.18 mm/s; (green, 36.0%) δ = 0.74 mm/s, ΔE_Q = 1.67 mm/s, γ = 0.14 mm/s.

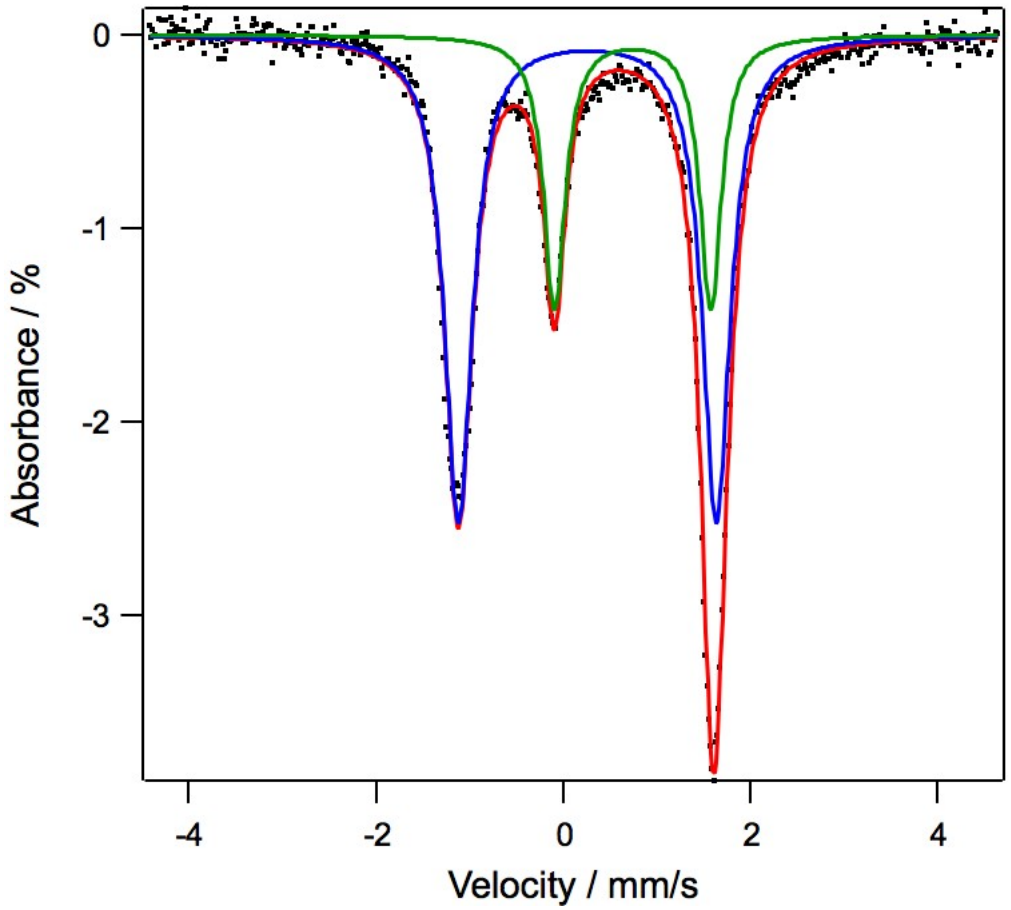

Figure S11. Zero-field ^{57}Fe Mössbauer spectrum of **6**. Simulation yields the following parameters: (blue, 64.3%) δ = 0.22 mm/s, ΔE_Q = 2.70 mm/s, γ = 0.15 mm/s; (green, 35.7%) δ = 0.81 mm/s, ΔE_Q = 1.74 mm/s, γ = 0.14 mm/s.

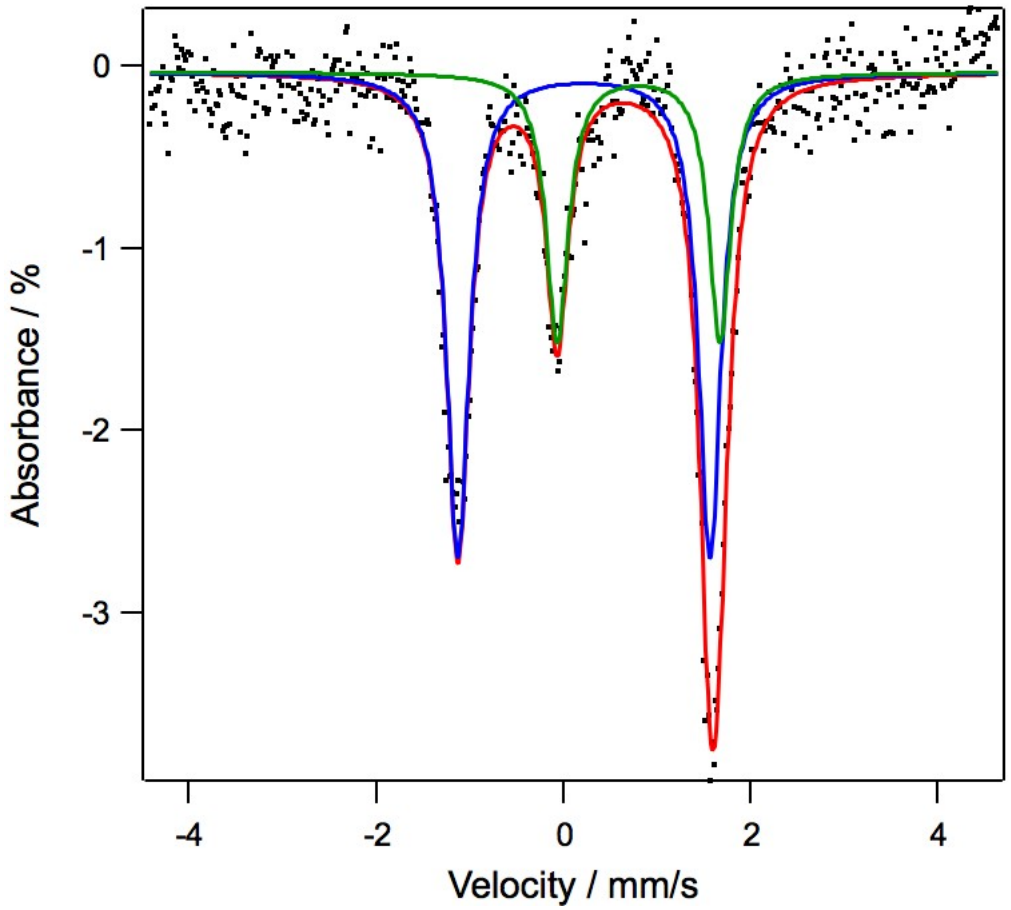

Figure S12. Variable-temperature magnetic susceptibility and reduced magnetization data for **2** with simulation parameters chosen to optimize reduced magnetization fit ($\boldsymbol{S}_1$ = 2, $\boldsymbol{S}_2$ = 3/2, J_1 = 15 cm^{-1}, J_2 = -1.5 cm^{-1}, D_1 = 40 cm^{-1}, D_2 = -120 cm^{-1}, g = 2.17 (susceptibility), g = 1.97 (reduced magnetization)).

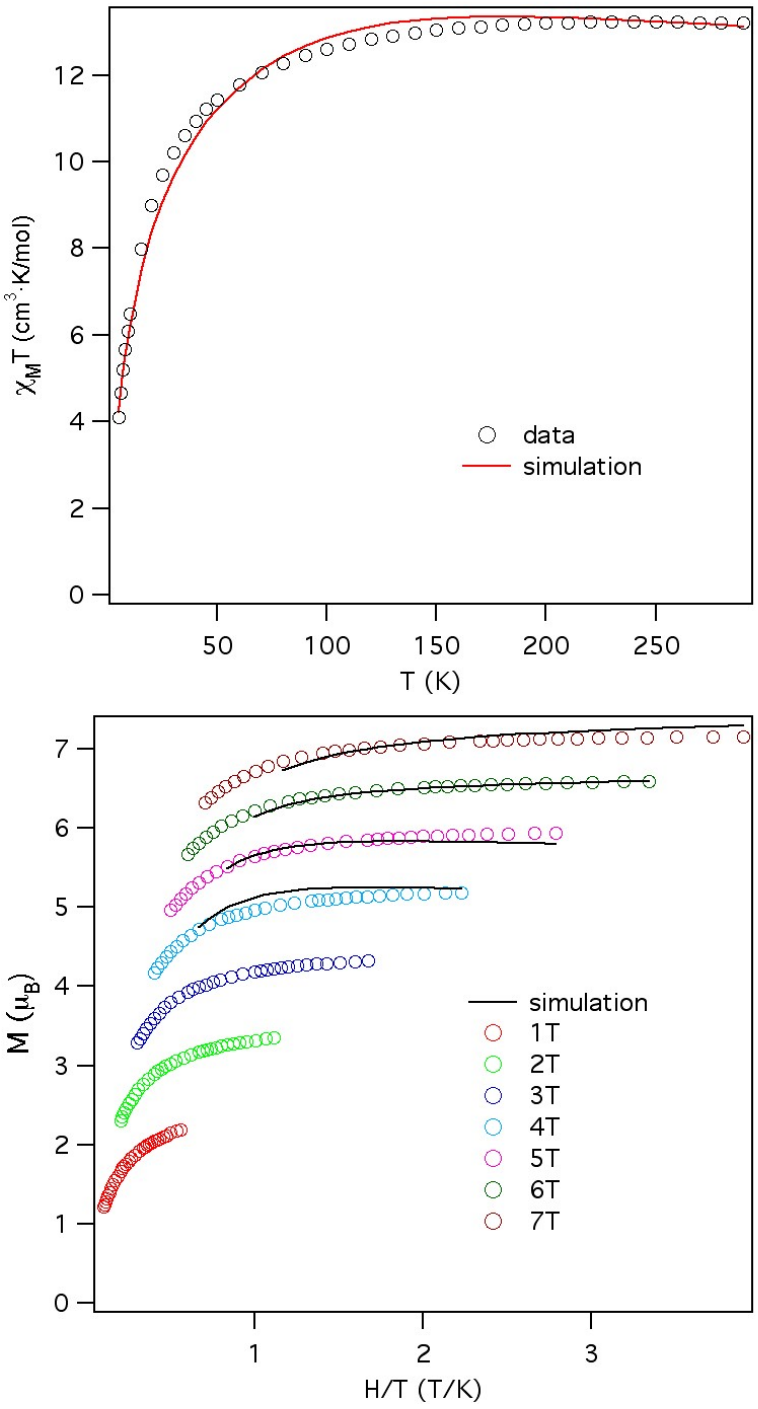

Figure S13. Variable-temperature magnetic susceptibility and reduced magnetization data for **3** with simulation ($\boldsymbol{S}_1$ = 2, $\boldsymbol{S}_2$ = 3/2, J = 16 cm^{-1}, D_1 = 36 cm^{-1}, D_2 = -47 cm^{-1}, g = 2.09 (susceptibility), g = 2.02 (reduced magnetization)).

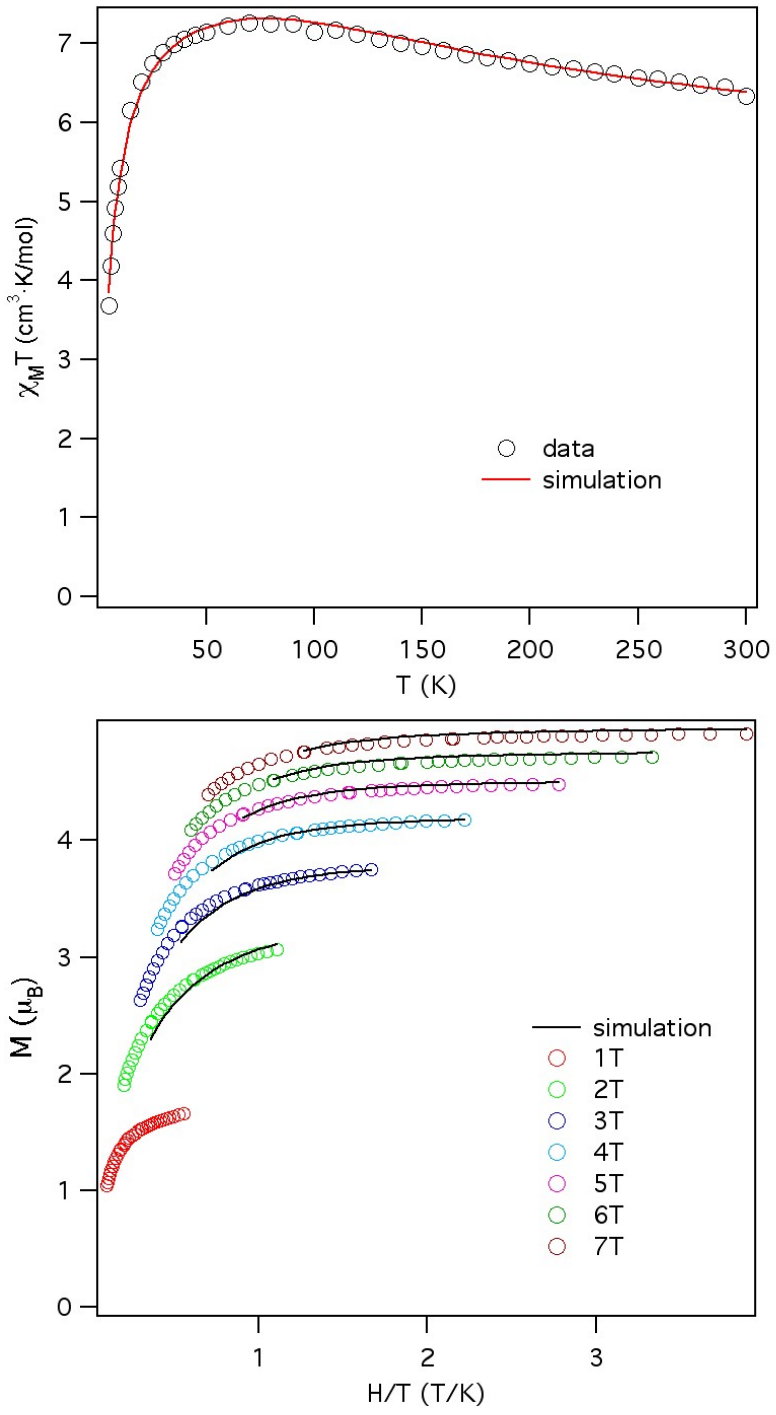

Figure S14. Variable-temperature magnetic susceptibility and reduced magnetization data for **4** with simulation parameters chosen to optimize reduced magnetization fit ($\boldsymbol{S}_1$ = 2, $\boldsymbol{S}_2$ = 3/2, J_1 = 20 cm^{-1}, J_2 = -1.25 cm^{-1}, D_1 = 43 cm^{-1}, D_2 = -95 cm^{-1}, g = 2.28 (susceptibility), g = 2.08 (reduced magnetization)).

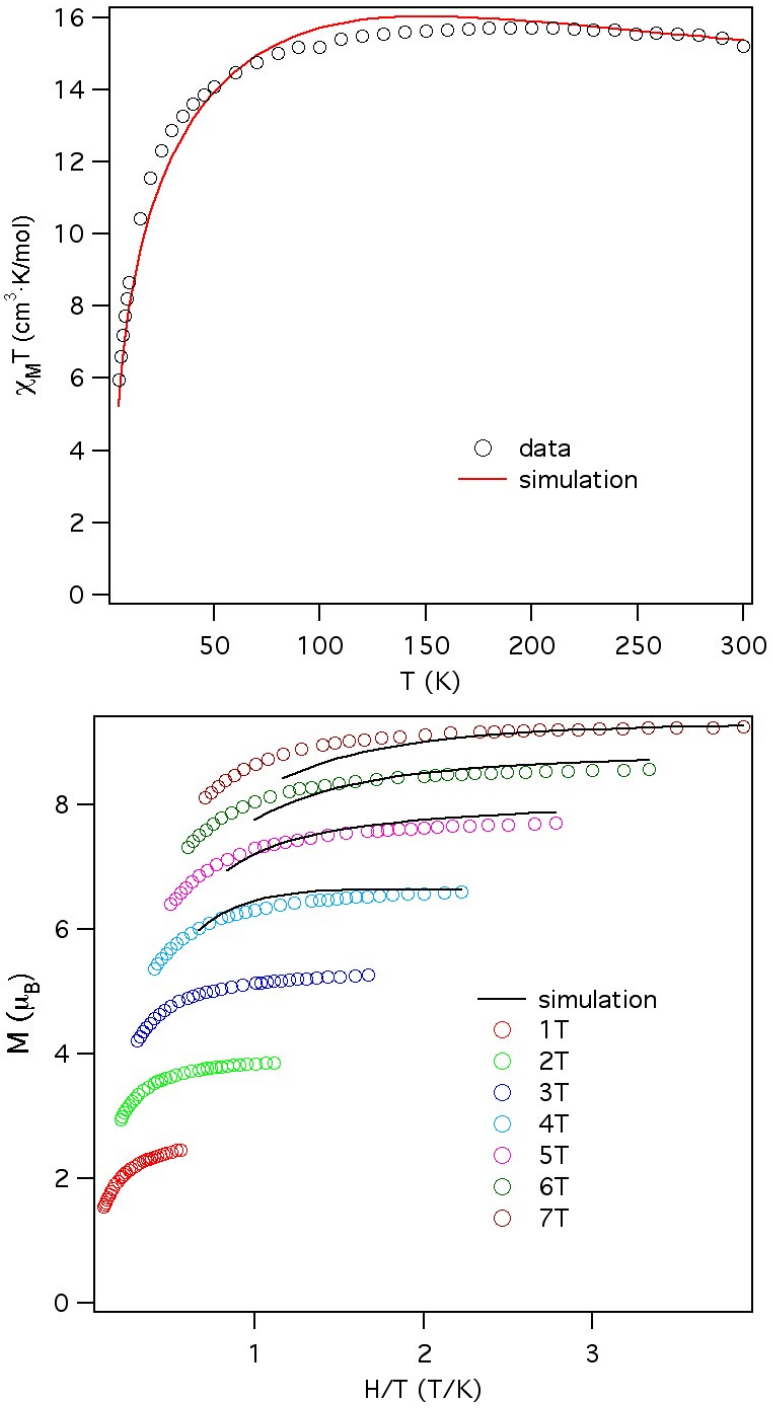

Figure S15. Variable-temperature magnetic susceptibility and reduced magnetization data for **5** with simulation ($\boldsymbol{S}_1 = 2$, $\boldsymbol{S}_2 = 3/2$, $J = 12.5$ cm^{-1}, $D_1 = 14$ cm^{-1}, $D_2 = -96$ cm^{-1}, $g = 2.23$ (susceptibility), $g = 2.00$ (reduced magnetization)).

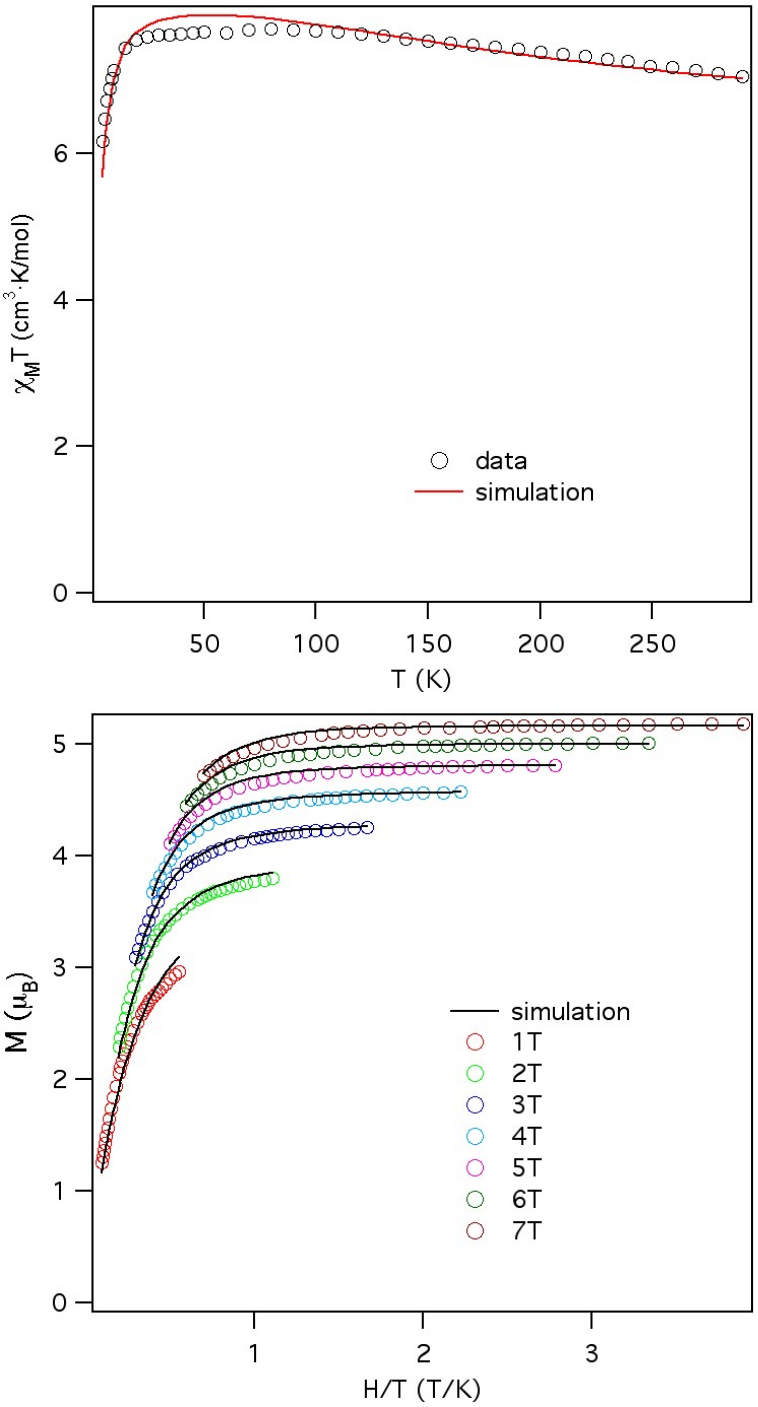

Figure S16. Variable-temperature magnetic susceptibility and reduced magnetization data for **6** with simulation ($\boldsymbol{S}_1 = 2$, $\boldsymbol{S}_2 = 3/2$, $J = 15$ cm^{-1}, $D_1 = 14$ cm^{-1}, $D_2 = -110$ cm^{-1}, $g = 2.01$ (susceptibility), $g = 1.79$ (reduced magnetization)).